



1           **The Improved Comparative Reactivity Method (ICRM):**  
2           **measurements of OH reactivity at high-NO<sub>x</sub> conditions in**  
3           **ambient air**

4  
5           **Wenjie Wang<sup>1,3#</sup>, Jipeng Qi<sup>1,2#</sup>, Jun Zhou<sup>1,2</sup>, Bin Yuan<sup>1,2\*</sup>, Yuwen Peng<sup>1,2</sup>, Sihang**  
6           **Wang<sup>1,2</sup>, Jonathan Williams<sup>4</sup>, Vinayak Sinha<sup>5</sup>, Min Shao<sup>1,2</sup>**

7  
8           <sup>1</sup>Institute for Environmental and Climate Research, Jinan University, Guangzhou  
9           511443, China.

10          <sup>2</sup>Guangdong-Hongkong-Macau Joint Laboratory of Collaborative Innovation for  
11          Environmental Quality, Guangzhou 511443, China.

12          <sup>3</sup>Multiphase Chemistry Department, Max Planck Institute for Chemistry, Mainz 55128,  
13          Germany.

14          <sup>4</sup>Atmospheric Chemistry Department, Max Planck Institute for Chemistry, Mainz  
15          55128, Germany.

16          <sup>5</sup>Department of Earth and Environmental Sciences, Indian Institute of Science  
17          Education and Research (IISER), Mohali 140306, India.

18

19

20          #W.J.W. and J.P.Q. contributed equally to this work.

21          \*Correspondence to: byuan@jnu.edu.cn

22



23 **Abstract**

24           The comparative reactivity method (CRM) has been developed more than a  
25 decade to measure OH reactivity (i.e. OH loss frequency) in both laboratory and field  
26 studies. However, accurate OH reactivity quantification remains challenging under real  
27 ambient condition, especially for OH reactivity measurements in high-NO<sub>x</sub> (e.g. >10  
28 ppbv) environments, as ambient NO enhance regeneration of OH radicals in the CRM  
29 reactor. To resolve this problem, we design a new improved CRM reactor (ICRM) and  
30 add NO into the system continuously, so that the HO<sub>2</sub> radical concentration is  
31 suppressed. We confirmed the appropriate level of NO by determining the maximum  
32 decrease in the pyrrole level caused by regenerated OH radicals from NO + HO<sub>2</sub>. VOC-  
33 induced RO<sub>2</sub> radicals in the ICRM reactor were also found to react with NO, which lead  
34 to the re-generation of OH radicals thus the underestimation of OH reactivity. This  
35 effect was quantified by the calibration of representative VOC species at different NO  
36 levels, and the correction coefficients obtained were used to correct the measured OH  
37 reactivity. All these efforts resulted in reducing the uncertainty of the NO-artifact  
38 correction by at least an order of magnitude compared to the original CRM system.  
39 Additionally, these technological improvements also considerably reduced the  
40 systematic errors from pyrrole photolysis that exists in the original system. A new  
41 operation mode was proposed for ICRM, which is able to avoid the interference  
42 resulting from OH radicals produced by photolysis of residual humidity and save time  
43 for ambient measurement. The ICRM system was employed in a field campaign to  
44 measure OH reactivity and performed well with ambient NO levels ranged from 0 to  
45 50 ppbv, which were typically observed in urban and suburban atmosphere.



## 46 **1 Introduction**

47 The hydroxyl radical (OH) is the most important oxidant in the daytime  
48 troposphere. It initiates the chemical removal of primary gaseous pollutants and in  
49 turn produces a host of secondary pollutants (A. Hofzumahaus, 1991; Atkinson, 2000;  
50 Roger Atkinson, 2003). The OH reactivity is defined as the sum of all OH reactive trace  
51 gas concentrations multiplied by their respective reaction rate coefficients with OH, as  
52 shown in Eq. 1. The OH reactivity is a fundamental property of the atmosphere in that  
53 it defines the overall loss frequency of OH radicals and hence the lifetime of OH. As  
54 such it is a useful atmospheric parameter for evaluating the level of reactive pollutants  
55 and it is closely related to atmospheric oxidation capacity and formation of secondary  
56 pollutants including ozone and secondary aerosols (Sinha et al., 2012; Yang et al., 2016;  
57 Pfannerstill et al., 2019).

$$58 \quad R_{OH} = \sum_i^n k_{VOC_i}[VOC_i] + k_{CO}[CO] + k_{NO_2}[NO_2] + k_{SO_2}[SO_2] + k_{O_3}[O_3] \quad (1)$$

59 Equation 1 defines the OH reactivity where  $R_{OH}$  is the total OH reactivity,  $k_{CO}$ ,  
60  $k_{NO}$ ,  $k_{NO_2}$ ,  $k_{SO_2}$ ,  $k_{O_3}$ , and  $k_{VOC_i}$  represent the reaction rate coefficients between OH  
61 radicals and CO, NO, NO<sub>2</sub>, SO<sub>2</sub>, O<sub>3</sub>, and volatile organic compounds (VOCs) species  
62  $i$ , respectively. [CO], [NO], [NO<sub>2</sub>], [SO<sub>2</sub>], [O<sub>3</sub>], and [VOC <sub>$i$</sub> ] are the concentrations of  
63 CO, NO, NO<sub>2</sub>, SO<sub>2</sub>, O<sub>3</sub>, and VOCs species  $i$ , respectively.

64 Currently, two general methods are used to measure OH reactivity: (1) direct  
65 measurements of OH decay rates by laser-induced fluorescence (LIF) technique; (2)  
66 measuring the relative change of a reference substance with and without ambient air  
67 present by the comparative reactivity method (CRM). The LIF based technology has  
68 been used to measure OH reactivity in a variety of different environments and has  
69 provided many new insights into the budget of OH reactivity (Kovacs et al., 2001;  
70 Kovacs et al., 2003; Sadanaga et al., 2004; Sadanaga et al., 2005; Ingham et al., 2009;  
71 Lou et al., 2010). However, the cost, complexity, and large size of LIF systems are  
72 deterrents to the widespread deployment for field measurements (Sinha et al., 2008).  
73 Such detector systems need to be built and cannot be bought directly from a supplier.



74 The CRM method measures OH decay rate indirectly by using the relative reaction rate  
75 of a reference substance (pyrrole) with self-generated OH radicals in the presence and  
76 absence of ambient air. The reference substance can be measured by an online  
77 instrument, such as proton transfer reaction mass spectrometry (PTR-MS) (Sinha et al.,  
78 2008; Sinha et al., 2009; Kumar et al., 2014) or a gas chromatograph (Nolscher et al.,  
79 2012a; Praplan et al., 2017a; Praplan et al., 2019b). The CRM technique has proven to  
80 be a useful supplementary technique to measure the total OH reactivity in ambient air,  
81 with a more economical and portable setup than the LIF-based systems. Based on inter-  
82 comparison between various OH reactivity techniques in the SAPHIR chamber, the LIF  
83 type-instruments are generally more sensitive and less noisy than CRM instruments  
84 (Fuchs et al., 2017).

85 The CRM approach has been applied to numerous field campaigns in recent years  
86 to measure OH reactivity (Dolgorouky et al., 2012; Nölscher et al., 2014; Michoud et  
87 al., 2015; Kim et al., 2016; Zannoni et al., 2016; Praplan et al., 2017b; Yang et al., 2017a;  
88 Zannoni et al., 2017; Kumar et al., 2018; Pfannerstill et al., 2018; Pfannerstill et al.,  
89 2019; Praplan et al., 2019a). However, this method is not suitable for the environment  
90 with high-level NO<sub>x</sub>, due to the pen-ray mercury lamp used to generate OH radicals in  
91 CRM system also generates approximately equivalent amounts of HO<sub>2</sub> radicals that  
92 may react with sampled NO to produce additional OH radicals (Sinha et al., 2008; Yang  
93 et al., 2017a), which cause an enhanced consumption of pyrrole in the CRM system and  
94 result in an underestimation of OH reactivity in sampled ambient air when NO exceeds  
95 certain levels (Sinha et al., 2008). This NO interference prevents the CRM method from  
96 providing high-quality data in emission exhausts and urban areas with high NO levels.  
97 As a result, applications of the CRM method have been generally restricted to high  
98 reactivity/low NO<sub>x</sub> environments, including forests (Sinha et al., 2010; Kim et al., 2011;  
99 Nolscher et al., 2012b; Praplan et al., 2019b; Pfannerstill et al., 2020), moderately  
100 polluted cities (NO < 10 ppb) (Sinha et al., 2008; Praplan et al., 2017b), pristine marine  
101 environments (Sinha et al., 2012; Zannoni et al., 2015), emission sources (e.g. gasoline  
102 evaporation) (Wu et al., 2015), branch cuvette studies (Nölscher et al., 2013), and



103 chamber studies (Nölscher et al., 2014) with little or no NO<sub>x</sub> present. One solution to  
104 this issue is to deliberately remove NO, before the sampled air is introduced into the  
105 reactor. However, the present technology is not able to remove NO selectively without  
106 affecting other reactive species (i.e., VOCs). The effect of NO on measured OH  
107 reactivity can be quantified by NO-correction experiments and the resulting correction  
108 curve applied to adjust ambient measurements according to simultaneously measured  
109 NO levels (Hansen et al., 2015; Yang et al., 2017a). However, the uncertainty of  
110 measured OH reactivity due to NO correction increases with NO concentration (Hansen  
111 et al., 2015; Michoud et al., 2015). Hansen et al. (2015) reported that the total  
112 uncertainty increases by up to a factor of 3 at NO<sub>x</sub> mixing ratios higher than 40 ppbv.  
113 Therefore, it calls for an improvement of the traditional CRM reactor for accurately  
114 quantifying OH reactivity at high NO<sub>x</sub> conditions. In addition to the NO effect,  
115 photolysis of pyrrole and VOCs, and the humidity difference between zero air and  
116 ambient air also influence measured OH reactivity (Sinha et al., 2008; Hansen et al.,  
117 2015; Zannoni et al., 2015).

118 The main purpose of this study is to improve the original CRM system to make it  
119 suitable for using in high-NO<sub>x</sub> conditions. We modified the structure of the original  
120 CRM glass reactor and add a certain amount of NO into the system to remove the  
121 generated but unwanted HO<sub>2</sub> radicals. We further characterized the improved CRM  
122 (ICRM) system by quantitatively evaluating the effect of the reaction of sample VOC-  
123 induced RO<sub>2</sub> with NO on measured OH reactivity. Additionally, the interference of  
124 pyrrole photolysis was also systematically evaluated. Finally, the ICRM system was  
125 deployed to measure OH reactivity under high-NO<sub>x</sub> conditions (0-50 ppbv) during a  
126 field campaign in the Pearl River Delta region of China.

## 127 **2 Experimental and Methodology**

### 128 **2.1 The original CRM reactor**

129 The schematic of the original CRM reactor is shown in Fig. 1a. Gas-phase pyrrole  
130 mixed with zero air or ambient air is introduced through arm C at a constant flow. Arm



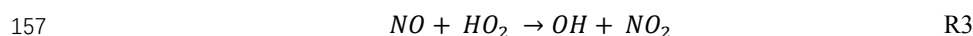
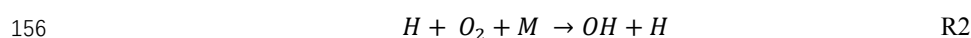
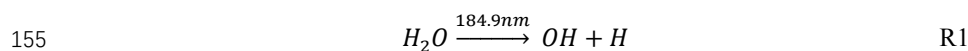
131 A consists of a pen-ray spectral mercury lamp, over which nitrogen (humidified or dry)  
132 is passed through arm B at a constant flow rate. When humidified nitrogen is flowing  
133 and the mercury lamp is turned on, H<sub>2</sub>O is photolyzed into OH and H radicals by the  
134 mercury lamp at 184.9 nm. The total air flow in the reactor exits through arm F and the  
135 concentration of pyrrole is monitored with a PTR-MS. A detailed description of the  
136 original CRM method has been reported by Sinha et al. (2008).

137 Figure 1(b) shows the four work modes of the original CRM method (Sinha et al.,  
138 2009). In C0 mode, the mercury lamp is turned off and high-purity dry nitrogen is  
139 introduced into the reactor through arm B. Pyrrole is introduced into the reactor with  
140 dry zero air through arm C. In C1 mode, the mercury lamp is turned on while everything  
141 else remains the same as C0. Pyrrole concentration decreases during C1 mode due to  
142 its photolysis reaction. In C2 mode, nitrogen flow in C1 is changed to humidified  
143 nitrogen to generate OH radicals, and the pyrrole concentration decreases to C2. In the  
144 final step, ambient air is introduced to the reactor through arm C in C3 mode. Based on  
145 pseudo-first-order assumptions (i.e., [pyrrole] ≥ [OH]), total OH reactivity ( $R_{OH}$ ) is  
146 calculated as Eq. 2:

$$147 \quad R_{OH} = C1 \times k_{pyr+OH} \times \frac{C3-C2}{C1-C3} \quad (2)$$

148 Where  $k_{pyr+OH}$  is the rate coefficient for the reaction of pyrrole with OH radicals  
149 ( $1.28 \times 10^{-10} \text{ cm}^3 \cdot \text{molecule}^{-1} \cdot \text{s}^{-1}$  (Dillon et al., 2012)), and C1, C2, and C3 represent  
150 pyrrole concentrations at the corresponding steps described above, respectively.

151 In C2 and C3 mode, OH radicals are produced by the photolysis of water vapor at  
152 atmospheric pressure as shown in R1. The generated H radicals from R1 reacts with O<sub>2</sub>  
153 of zero air or ambient air to generate HO<sub>2</sub> radicals, as shown in R2. When NO is present  
154 in the sampled ambient air, it can recycle OH by reacting with HO<sub>2</sub> (R3).



158 An underlying assumption of the CRM approach is that the influence of the species  
159 in ambient air on OH radicals in the reactor is ignorable. However, the additional OH



160 radicals produced via R3 can react with pyrrole to cause an additional decrease in  
161 pyrrole relative to C2 mode, thus lead to the underestimation of OH reactivity.

## 162 **2.2 The improved CRM reactor**

163 In order to remove the interference of the reaction of HO<sub>2</sub> radicals with NO as  
164 discussed above, we modified the pipe structure of the original CRM reactor (Fig. 1c).  
165 We kept the length and volume of the glass reactor of the ICRM system similar to the  
166 original CRM system, but added a branch inlet G (1/4 inch OD glass; length 3 cm) in  
167 arm A to introduce steam of NO standard (Air Liquide; stated uncertainty 3%; 10.8  
168 ppmv) mixed with zero air at a constant flow of 120 ml·min<sup>-1</sup>. The typical flow rate  
169 inside the ICRM reactor is approximately 660 ml·min<sup>-1</sup>. The flow rate of nitrogen (Air  
170 Liquide; 99.9995% purity) through arm B is 250 ml·min<sup>-1</sup>. The input pyrrole (Linde  
171 Spectra Environment Gases; stated uncertainty 5%; 5.37 ppm) flow rate is 2.5 ml·min<sup>-1</sup>.  
172 The total flow rate of pyrrole and zero air (Air Liquide; 99.9995% purity) through  
173 arm C is 290 ml·min<sup>-1</sup>. With this modified structure of arm A, the HO<sub>2</sub> radicals,  
174 produced by the reaction of the generated H radicals near the mercury lamp and O<sub>2</sub> in  
175 introduced zero air, were converted to OH radicals by reacting with NO in the  
176 downstream of arm G. The interference induced by R3 can then be eliminated.

177 Arm A consists of one 1/2 inch OD (ID: 0.62 cm, length: 7 cm) glass tube and one  
178 1/4 inch OD (ID: 0.32 cm, length: 5 cm) glass tube. The purpose of this structure is to  
179 ensure that the UV light is mostly confined within a 1/2 inch OD glass tube of arm A,  
180 as the diameter of arm A goes from wide to slender. The new structure of arm A leads  
181 to lower OH concentrations (decreased by approximately 50%) passing into reactor due  
182 to wall loss, OH radicals produced from the reaction of HO<sub>2</sub> radicals with NO can  
183 partially compensate for this loss.

## 184 **2.3 The detection of pyrrole by PTR-MS**

185 The accuracy of pyrrole measurement is critical in determining OH reactivity for  
186 CRM method. Here we used PTR-MS to detect pyrrole concentration. With a proton  
187 affinity greater than water (Pyrrole: 209.2 kcal·mol<sup>-1</sup>; Water: 165.2 kcal·mol<sup>-1</sup>) (Sinha



188 et al., 2008), pyrrole is chemically ionized by proton transfer with  $\text{H}_3\text{O}^+$  ions and the  
189 product ions are detected using a quadrupole mass spectrometer. As highlighted by  
190 Sinha et al. (2009), the sensitivity of PTR-MS instruments toward pyrrole is dependent  
191 on humidity, and the pyrrole signal must be carefully calibrated for relative humidity  
192 changes within the CRM reactor. The approach described by de Gouw and Warneke  
193 (2007) was employed in this study to account for the effect of ion source and humidity  
194 on the sensitivity of PTR-MS toward pyrrole (de Gouw et al., 2007). This approach  
195 involves normalization of the pyrrole signal to a sum of reagent ion signals ( $\text{H}_3\text{O}^+ + X_R$   
196  $\times \text{H}_3\text{O}^+ \cdot \text{H}_2\text{O}$ ) that leads to a normalized signal for pyrrole that is independent of  
197 humidity.  $X_R$ , a scaling factor for the  $\text{H}_3\text{O}^+ \cdot \text{H}_2\text{O}$  signal, is determined experimentally  
198 by measuring the pyrrole signal from a standard mixture under different humidity  
199 conditions. In this study, a relatively higher electric field parameter of the drift tube (i.e.  
200  $E/N$ ) value of 153 Td was used to measure pyrrole, which can minimize the humidity  
201 effect from water clusters in the PTR-MS instrument. As shown in SI, the best estimate  
202 for  $X_R$  parameter was determined to be zero (Fig. S1), indicating negligible role for  
203  $\text{H}_3\text{O}^+ \cdot \text{H}_2\text{O}$  in pyrrole detection by PTR-MS in this study.

#### 204 **2.4 Other instruments of the ambient measurement campaign**

205 In order to test and validate the ICRM system for OH reactivity measurements  
206 under high NO concentrations, we conducted field measurements of OH reactivity at a  
207 receptor site in the Pearl River Delta (PRD) region of China (Yang et al., 2017b; Tan et  
208 al., 2019). Meanwhile, non-methane hydrocarbons (NMHCs) and oxygenated volatile  
209 organic compounds (OVOCs) were also measured by online gas chromatograph mass  
210 spectrometer and flame ionization detector (GC-MS/FID) (Wang et al., 2014a) and  
211 proton transfer reaction time-of-flight mass spectrometry (PTR-TOF-MS) (Yuan et al.,  
212 2017), respectively (Table S1). Inorganic trace gases, including CO, NO<sub>2</sub>, NO, SO<sub>2</sub> and  
213 O<sub>3</sub>, were measured by Thermofisher 48i CO analyzer, 2B Technologies Model 405nm  
214 NO<sub>x</sub> analyzer, Thermofisher 42i NO<sub>x</sub> analyzer, Thermofisher 43i SO<sub>2</sub> analyzer, and  
215 Thermofisher 49i O<sub>3</sub> analyzer, respectively. Detailed descriptions of these systems can  
216 be found in previous studies (Wang et al., 2014b; Birks et al., 2018).





## 217 **2.5. Zero dimensional box model**

218 To test our understanding of the chemical processes occurring inside the ICRM  
219 reactor, results from laboratory experiments were compared with simulation from zero-  
220 dimensional (0-D) box model. The MCM v3.3.1 (Wolfe et al., 2016) was used as  
221 chemical mechanism in the box model. The use of the detailed mechanism aims at better  
222 representing the chemistry of peroxy radicals. In the box model, the initial  
223 concentrations of OH, HO<sub>2</sub>, pyrrole, VOCs, CO, and NO were supplied, and the time-  
224 dependent variations of different compounds in the reactor are simulated. The initial  
225 concentrations of OH (4 ppbv), HO<sub>2</sub> (4 ppbv), and pyrrole (21 ppbv) are determined  
226 based on results from our experiments. The residence time in the reactor was about 11  
227 s according to the volume of the reactor (120 cm<sup>3</sup>) and the flow of introduced gases  
228 (660 ml·min<sup>-1</sup>). An MCM subset was extracted for inorganic reactions, and reactions  
229 for propane, propene, and toluene. C<sub>3</sub>H<sub>5</sub>O<sub>2</sub> was used as a surrogate for the peroxy  
230 radicals from pyrrole, as the degradation of pyrrole is not included in MCM.

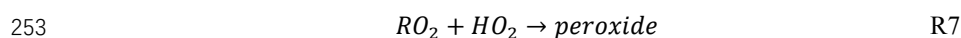
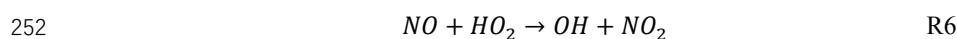
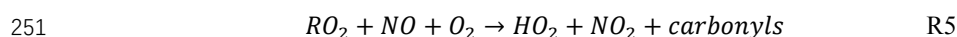
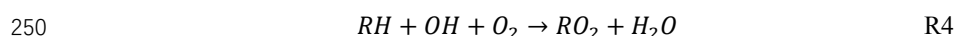
## 231 **3 Results and discussion**

### 232 **3.1 Determination of the amount of NO addition**

233 In addition to HO<sub>2</sub> produced from the reaction of H radicals with O<sub>2</sub>, RO<sub>2</sub> produced  
234 from the reaction of pyrrole with OH also react with NO to recycle HO<sub>2</sub> and OH (R4-  
235 R6), and consume pyrrole. In order to eliminate the effect of HO<sub>2</sub> and RO<sub>2</sub> radicals, NO  
236 supply with an appropriate concentration through arm G is needed. We optimized NO  
237 concentration by testing the dependence of the change of the pyrrole concentrations on  
238 the concentration of NO introduced through arm G (as described below and Fig. 2).  
239 During the experiment, the pyrrole concentration in the C1 mode (where N<sub>2</sub> and zero  
240 air were humidified and mercury lamp is turned off) was 22 ppbv, which decreased to  
241 18 ppbv when the mercury lamp was turned on at 0 ppbv NO, implying that the  
242 generated OH radicals depleted ~ 4 ppbv pyrrole. We varied the NO concentrations  
243 mixed with the zero air entering arm G which resulted in NO concentrations in the  
244 reactor ranged from 0 to 150 ppbv, and found out the appropriate NO level to consume



245 all HO<sub>2</sub> and RO<sub>2</sub> produced in the glass reactor. NO was mixed with zero air rather than  
246 nitrogen, as oxygen in zero air can transform H radicals in arm A to HO<sub>2</sub> radicals.  
247 Pyrrole concentration decreases with the increase of NO concentrations, reaching a  
248 minimum when NO concentration is circa 40 ~ 50 ppbv, and increased again when NO  
249 concentration exceeds 50 ppbv.



254 where RH represents pyrrole in the reactor or introduced ambient VOCs into the reactor.

255 The NO addition experiments are simulated in the box model. The simulated  
256 pyrrole concentrations as a function of NO concentration is consistent with laboratory  
257 experiments: with pyrrole concentrations decreasing at first and then increasing (Fig.  
258 S2). When NO is not present in the reactor, the self-reactions of peroxy radicals  
259 (HO<sub>2</sub>+HO<sub>2</sub>, HO<sub>2</sub>+RO<sub>2</sub>) dominate the sink of HO<sub>2</sub> and RO<sub>2</sub> (Fig. S3). As NO is  
260 introduced into the reactor, the reaction of NO with HO<sub>2</sub> or RO<sub>2</sub> competes with the self-  
261 reactions of peroxy radicals. With more NO introduced, the produced OH radicals from  
262 the reaction of HO<sub>2</sub> with NO increase, leading to the decrease of pyrrole concentration  
263 (Fig. S3). As the NO concentration exceeds 50 ppbv, pyrrole concentrations increase  
264 again, due to the large excess NO competes with pyrrole for reaction with OH radicals.  
265 The remaining NO concentration outflowing from the reactor increases with the  
266 introduced NO concentrations (Fig. S2), indicating that excessive NO is needed to  
267 compete with the self-reactions of peroxy radicals. Based on laboratory measurement,  
268 the remaining NO concentration outflowing from the reactor is ~18 ppbv when the  
269 introduced NO concentration at 50 ppbv. The laboratory measurements and simulated  
270 results both suggest that 40 ~ 50 ppbv is the lowest NO concentration needed to  
271 transform HO<sub>2</sub> and RO<sub>2</sub> to OH to the largest extent. The higher introduced NO  
272 concentration had a negligible effect on the increase in OH production from HO<sub>2</sub> and  
273 RO<sub>2</sub>. Thus, we introduce 50 ppbv NO concentration into the ICRM reactor in the



274 experiments in this study. Under this optimized condition, the pyrrole concentration  
275 decreased to 12.3 ppbv. The concentration of pyrrole in this scenario is regarded as the  
276 C2 mode for ICRM system. It worth noting that the determined NO concentration can  
277 vary slightly as OH generation performance changes (e.g. humidity change in the region  
278 of the pen-ray mercury lamp).

279 Under the determined optimal NO level through arm G, it is necessary to ensure  
280 that the OH production from HO<sub>2</sub> and pyrrole-induced RO<sub>2</sub> will not manifest itself  
281 when ambient NO is introduced through arm C. For this purpose, we compared  
282 measured and true OH reactivity of NO by passing a series of NO concentrations (0 ~  
283 160 ppbv) mixed with zero air through arm C into the reactor (Figure 3). In this test, no  
284 other reactive gases were introduced into the system except NO. Measured OH  
285 reactivity of NO agreed well with the corresponding calculated values, indicating that  
286 HO<sub>2</sub> radicals have been fully consumed, and pyrrole peroxy radicals were effectively  
287 converted to carbonyls and nitrates by NO introduced through arm G.

### 288 3.2 Calibration for OH reactivity of VOCs

289 Several reactive VOC species were used to validate and calibrate the ICRM system,  
290 including propane, propene, toluene, and mixed gases including 16 VOC species  
291 (acetaldehyde, methanol, ethanol, isoprene, acetone, acetonitrile, methyl vinyl ketone,  
292 methyl ethyl ketone, benzene, toluene, o-xylene,  $\alpha$ -pinene, 1,2,4-trimethylbenzene,  
293 phenol, m-cresol, naphthalene). These VOC species were introduced into the system  
294 through arm C at various reactivity (0 ~ 80 s<sup>-1</sup>). Figure 4 (a) presents the plots of the  
295 measured ( $R_{\text{meas}}$ , s<sup>-1</sup>) versus true OH reactivity ( $R_{\text{true}}$ , s<sup>-1</sup>) of these species.  $R_{\text{meas}}$  is lower  
296 than  $R_{\text{true}}$  for almost all species with the slopes of linear fittings ranging from 0.70 to  
297 0.74. The slopes of propane, propene, toluene, and mixed gases are 0.70, 0.74, 0.72,  
298 and 0.72, respectively. The OH reactivity calibration of SO<sub>2</sub> and CO indicates that the  
299 linear fitting slope of  $R_{\text{meas}}$  versus  $R_{\text{true}}$  is 0.33 and 0.41, respectively (Fig. 4 b), which  
300 is lower than that of VOCs.

301 Equation 2 is valid only under near pseudo-first-order conditions (i.e. when  
302 [pyrrole]  $\gg$  [OH]). In this study, the [pyrrole] to [OH] ratio is set at 2.5, which will



303 cause significant systematic errors. We plot the calculated reactivity, obtained by  
304 applying Eq. 2 to the numerical simulations of the pyrrole concentration (C2 and C3)  
305 at  $[\text{Pyrrole}]/[\text{OH}] = 2.5$  after OH had reacted to zero, versus the true reactivity. The  
306 correction curve indicates that the calculated reactivity underestimates the true  
307 reactivity by about 5%. After considering this interference, the slope of calibration  
308 shown in Fig. 4 (a) and 4(b) decreased to 0.66 ~ 0.70 for VOCs, 0.31 for SO<sub>2</sub> and 0.39  
309 for CO, respectively. Therefore, the deviation of pseudo-first-order conditions cannot  
310 explain the calibrated slopes for VOCs, CO and SO<sub>2</sub> being lower than one.

311 The lower calibrated slopes for VOCs than one can be related to secondary  
312 chemistry of VOC-generated RO<sub>2</sub> radicals with NO. When more VOCs are introduced  
313 into the reactor, additional RO<sub>2</sub> radicals produced from the reaction of VOCs with OH  
314 will react with excessive NO in the reactor thus increase the recycled OH (R4-R6). The  
315 recycled OH from RO<sub>2</sub> will deplete pyrrole thus leading to a  $R_{\text{meas}}$  lower than the  $R_{\text{true}}$ .  
316 We deduce that this is the reason for the linear fitting slopes in Fig. 4 lower than one.  
317 For specific VOC species, the decrease in pyrrole concentration due to recycling OH  
318 depends on the true OH reactivity of VOCs, NO concentrations and the efficiency of  
319 organic nitrate production ( $\text{RO}_2 + \text{NO} \rightarrow \text{RONO}_2$ ) in this system. The consistency in  
320 the linear fitting slopes of different VOC species indicate that the RO<sub>2</sub> + NO reactions  
321 for the investigated VOCs are similar. This is in agreement with the simulated results  
322 (Fig. S7). The lower fitting slope of SO<sub>2</sub> and CO than that of VOCs is because SO<sub>2</sub> and  
323 CO react with OH to produce HO<sub>2</sub>, which has higher efficiency to produce OH by  
324 reacting with NO than RO<sub>2</sub> that goes through two steps (RO<sub>2</sub>→HO<sub>2</sub>, and HO<sub>2</sub>→OH).  
325 Here, we define the linear fitting slopes in Fig. 4 as correction coefficients with regard  
326 to the calibration for OH reactivity of VOC, CO and SO<sub>2</sub> (characterized by  $\alpha_{\text{VOC}}$ ,  $\alpha_{\text{CO}}$   
327 and  $\alpha_{\text{SO}_2}$ ) at ambient NO = 0 ppbv.

328 To further evaluate the performance of the ICRM system with elevated NO<sub>x</sub>  
329 concentrations in ambient air, a series of NO concentrations were introduced into the  
330 reactor through arm C both with constant reactivity from different VOC species and  
331 with different reactivities provided by the same species. Of all experimental conditions,



332 the  $R'_{\text{meas}}$  (The  $R'_{\text{meas}}$  is defined as the corrected  $R_{\text{meas}}$  by correction coefficient  $\alpha_{\text{VOC}}$ )  
333 was observed to decrease with increased NO concentration (Fig. S5), and thus the  
334 difference between  $R_{\text{true}}$  and  $R'_{\text{meas}}$  ( $R_{\text{true}} - R'_{\text{meas}}$ ) increases with increased NO  
335 concentrations for the four VOC standard gases (Fig. 5a and b). This is because the  
336 reaction rate of RO<sub>2</sub> with NO increases with NO concentrations leading to enhancement  
337 of the recycled OH. The linear fitting slopes of ( $R_{\text{true}} - R'_{\text{meas}}$ ) versus NO concentrations  
338 for different VOC species and different reactivity levels range from 0.10 to 0.22 s<sup>-1</sup>  
339 ppbv<sup>-1</sup>. Similar to VOCs, the difference between  $R_{\text{true}}$  and  $R'_{\text{meas}}$  ( $R_{\text{true}} - R'_{\text{meas}}$ ) also  
340 increases with NO concentrations for CO and SO<sub>2</sub> with slope of 0.11 and 0.10  
341 respectively (The  $R'_{\text{meas}}$  is defined as the corrected  $R_{\text{meas}}$  by correction coefficient  $\alpha_{\text{CO}}$   
342 and  $\alpha_{\text{SO}_2}$ ) (Fig. 5 c). However, the difference of NO effects between VOCs and CO (and  
343 SO<sub>2</sub>) as shown in Fig. 4 and Fig. 5 has not been reported in previous studies about CRM  
344 system.

345 Previous studies have reported that NO had a large effect on the difference between  
346  $R_{\text{true}}$  and  $R_{\text{meas}}$  in the CRM systems (Note that the  $R_{\text{meas}}$  is not corrected in previous  
347 studies) (Hansen et al., 2015; Michoud et al., 2015; Yang et al., 2017b). This NO-effect  
348 is not only due to the reaction of HO<sub>2</sub> with NO, but also due to the reaction of pyrrole-  
349 produced and VOC-produced RO<sub>2</sub> with NO. Figure S6 compares the effect of NO on  
350 ( $R_{\text{true}} - R_{\text{meas}}$ ) in the original CRM system (reported by previous studies) with that in the  
351 ICRM system (this study). Far larger NO effects were reported in the original CRM  
352 system than in the ICRM system. For example, the presence of ambient NO at 50 ppbv  
353 leads to  $R_{\text{meas}}$  lower than the  $R_{\text{true}}$  by 70 ~ 240 s<sup>-1</sup>, at least an order of magnitude higher  
354 than the NO artifact in the ICRM system, which leads to  $R'_{\text{meas}}$  lower than the  $R_{\text{true}}$  by  
355 5 ~ 13 s<sup>-1</sup>. This is because both HO<sub>2</sub> and pyrrole-induced RO<sub>2</sub> are fully removed by the  
356 introduced NO in advance in the ICRM system, thus the remaining influencing factor  
357 is the reaction of ambient VOCs-induced RO<sub>2</sub> with NO. The uncertainty due to the NO-  
358 artifact correction in the ICRM system was predicted to be far lower than that of the  
359 original CRM system, as the absolute change of OH reactivity caused by NO is reduced  
360 by removing HO<sub>2</sub> and pyrrole-induced RO<sub>2</sub>. Despite the ICRM system not being able



361 to remove the NO effect entirely, it does lead to a significant decrease in the uncertainty  
362 of the NO-artifact correction.

363 Due to the different behaviors of VOCs, SO<sub>2</sub> and CO at high NO conditions, in  
364 order to get accurate OH reactivity, it is necessary to conduct NO-correction for VOCs,  
365 SO<sub>2</sub>, and CO individually. Note that this issue may also present in the original CRM  
366 system, but it was ignored in previous studies. For the ICRM system, we use the  
367 following formula to determine the true OH reactivity of VOCs:

$$368 R_{meas} = R_{true\ NO+NO_2} + R_{true\ O_3} + \alpha_{CO}(R_{true\ CO} - \beta_{CO}[NO]) + \alpha_{SO_2}(R_{true\ SO_2} - \\ 369 \beta_{SO_2}[NO]) + \alpha_{VOC}(R_{true\ VOC} - \beta_{VOC}[NO]) \quad (3)$$

$$370 R_{true\ VOC} = \frac{1}{\alpha_{VOC}}(R_{meas} - R_{true\ NO+NO_2} - R_{true\ O_3} + \alpha_{CO}\beta_{CO}[NO] + \\ 371 \alpha_{SO_2}\beta_{SO_2}[NO] + \alpha_{VOC}\beta_{VOC}[NO] - \alpha_{CO}R_{true\ CO} - \alpha_{SO_2}R_{true\ SO_2}) \quad (4)$$

372 where  $R_{meas}$  is the measured OH reactivity by the ICRM system as defined above.  
373 The  $R_{true\ VOC}$  is the true OH reactivity of VOCs.  $R_{i\ true}$  was calculated from measured  
374 concentrations of species  $i$  ( $i=NO, NO_2, O_3, SO_2$  and CO) multiplied by the rate  
375 coefficient of the reaction of species  $i$  with OH. The  $R_{meas}$  and  $R_{true}$  of NO<sub>x</sub> (=NO+NO<sub>2</sub>)  
376 was close to 1:1 as shown in Fig. 3 and S4.  $\alpha_{CO}$ ,  $\alpha_{SO_2}$ , and  $\alpha_{VOC}$  are the correction  
377 coefficients with regard to the calibration for OH reactivity of CO, SO<sub>2</sub> and VOC at  
378 ambient NO = 0 ppbv, respectively. Note that the  $\alpha_{VOC}$  is mean slope of Fig. 4 a  $\beta_{CO}$ ,  
379  $\beta_{SO_2}$ , and  $\beta_{VOC}$  are the correction coefficients which regard to the effect of ambient  
380 NO on ( $R_{true} - R'_{meas}$ ). Note that the  $\beta_{VOC}$  is mean slope of Fig. 5 a and b. After getting  
381  $R_{true\ VOC}$ , the total OH reactivity ( $R_{tot}$ ) was then calculated as the summation of  
382  $R_{true\ VOC}$ ,  $R_{true\ NO+NO_2}$ ,  $R_{true\ O_3}$ ,  $R_{true\ SO_2}$ , and  $R_{true\ CO}$ :

$$383 R_{tot} = R_{true\ VOC} + R_{true\ NO} + R_{O_3} + R_{true\ NO_2} + R_{true\ CO} + R_{true\ SO_2} \quad (5)$$

### 384 3.3 Additional potential interference related to NO addition

385 In order to assess the extent of any additional interferences due to NO addition,  
386 we further consider the following effects.

387 In arm A, the photolysis of O<sub>2</sub> introduced through arm G by the mercury lamp  
388 produces O<sub>3</sub>. Besides, the NO introduced through arm G reacts with HO<sub>2</sub> to generate



389 NO<sub>2</sub>, which can also photolysis to generate NO and oxygen atoms, and subsequently  
390 O<sub>3</sub>. We monitored O<sub>3</sub> concentration through the arm F using an O<sub>3</sub> monitor. O<sub>3</sub>  
391 concentration flowing out of arm F was less than 5 ppbv, which has a negligible  
392 influence on the pyrrole concentrations and the  $R_{\text{meas}}$ , considering the pyrrole+O<sub>3</sub>  
393 reaction rate constant  $k_{\text{O}_3+\text{pyrrole}} = 1.57 \times 10^{-17} \text{ cm}^3 \text{ molecule}^{-1} \text{ s}^{-1}$  (Atkinson et al., 1984)  
394 is several orders of magnitude slower than the pyrrole + OH reaction rate constant  
395 ( $k_{\text{pyrrole}+\text{OH}} = 1.28 \times 10^{-10} \text{ cm}^3 \text{ molecule}^{-1} \text{ s}^{-1}$ ). The ozone concentration was low, as excess  
396 NO was introduced to the reactor and the remaining NO titrates O<sub>3</sub> back to NO<sub>2</sub>.

397 In the C3 mode of the ICRM, sample ambient O<sub>3</sub> can react with the high-levels  
398 NO in the reactor, which might interfere with  $R_{\text{meas}}$ . We characterize this interference  
399 by introducing a series of O<sub>3</sub> concentrations into the reactor through arm C. As O<sub>3</sub>  
400 concentrations lower than 40 ppbv, O<sub>3</sub> has a negligible effect on OH reactivity (Fig. 6).  
401 Interestingly,  $R_{\text{meas}}$  first increases and then decrease with increasing O<sub>3</sub> concentrations.  
402 The reaction rate coefficient of OH with NO<sub>2</sub> is slightly higher than with NO, which  
403 are  $1.2 \times 10^{-11} \text{ cm}^3 \text{ molecule}^{-1} \text{ s}^{-1}$  and  $1.0 \times 10^{-11} \text{ cm}^3 \text{ molecule}^{-1} \text{ s}^{-1}$  at 298K, respectively  
404 (Atkinson et al., 2004). With the increase of introduced O<sub>3</sub> concentration, higher NO<sub>2</sub>  
405 is produced, which causes an increase in  $R_{\text{meas}}$ . As NO is consumed completely by O<sub>3</sub>,  
406 excessive O<sub>3</sub> can further react with NO<sub>2</sub> to produce NO<sub>3</sub> radicals, which can deplete  
407 pyrrole ( $k = 1.80 \times 10^{-10} \text{ cm}^3 \text{ molecule}^{-1} \text{ s}^{-1}$ ) (Cabanas et al., 2004) and lead to the  
408 decrease in  $R_{\text{meas}}$ . Overall, OH reactivity exhibited little change ( $< 2 \text{ s}^{-1}$ ) with the  
409 increase of O<sub>3</sub> concentrations (0 ~ 160 ppbv), indicating that the introduced O<sub>3</sub> plays a  
410 negligible role in  $R_{\text{meas}}$ . This is another advantage of ICRM compared with the original  
411 CRM, which needs an ozone correction as the reaction of O<sub>3</sub> with HO<sub>2</sub> gives OH back  
412 (Fuchs et al., 2017).

413 According to model simulation, the produced NO<sub>2</sub> from the reaction of NO with  
414 HO<sub>2</sub> increases with introduced NO concentrations (Fig. S2). The produced NO<sub>2</sub> can  
415 deplete OH ( $\text{OH} + \text{NO}_2 \rightarrow \text{HNO}_3$ ) and thereby lead to an increase in the pyrrole  
416 concentration. When introduced NO with a concentration of 50 ppbv, the produced NO<sub>2</sub>  
417 was 25 ppbv, corresponding to  $6.2 \text{ s}^{-1}$  OH reactivity (Fig. S2). However, this process



418 doesn't interfere with the  $R_{\text{meas}}$  as the produced  $\text{NO}_2$  is the same in both C2 and C3  
419 modes leading to this effect canceling out in the two modes.

### 420 **3.4 Photolysis of pyrrole**

421 Photolysis of pyrrole in the CRM method introduces additional uncertainties and  
422 complexity in the determination of OH reactivity (Sinha et al., 2008; Hansen et al.,  
423 2015; Michoud et al., 2015; Zannoni et al., 2015). To investigate the effect of the ICRM  
424 system on the interference from photolysis, we turn the mercury lamp off and on to test  
425 the variation in pyrrole concentrations under dry conditions (no humidification).  
426 Compared with the condition where the mercury lamp is turned off, pyrrole  
427 concentrations decreased by  $< 3\%$  after the mercury lamp was turned on (Fig. S8),  
428 which caused  $R_{\text{meas}}$  increase of  $0.55 \text{ s}^{-1}$  when the  $R_{\text{true}}$  was  $20 \text{ s}^{-1}$ . This result indicates  
429 that the photolysis of pyrrole is weak enough to be negligible in the ICRM system. This  
430 smaller photolysis of pyrrole closely relates to the improved design of reactor structure.  
431 Arm A consists of two section of glass tube with 1/2 inch OD and 1/4 inch OD,  
432 respectively (Fig. 1). UV light is mostly confined in 1/2 inch OD glass tube of arm A,  
433 as the glass tube is constructed with decreasing diameter following the direction of gas  
434 flow. This reduces the amount of UV light getting into the main reaction part of the  
435 reactor. The improved structure of arm A leads to lower OH concentrations (decreased  
436 by approximately 50%) passing into reactor due to wall loss, but the OH radicals  
437 produced from the reaction of  $\text{HO}_2$  radicals with NO can partially compensate for this  
438 loss. In comparison, the pen-ray mercury lamp was very close to the main body of the  
439 reactor in the original CRM reactor, to maximize the OH entering the reactor by  
440 minimizing wall loss. However, this will lead to the photolysis of pyrrole, as high as  
441 25% (Sinha et al., 2008; Hansen et al., 2015). The change of the structure of arm A also  
442 ensures that the photolysis of  $\text{H}_2\text{O}$ , HONO,  $\text{NO}_2$ , and VOCs inside the ICRM reactor is  
443 weaker than that in the original CRM system. In addition to our design change, previous  
444 studies have reported that the photolysis of pyrrole can be also lowered to below 5% by  
445 changing the UV mercury lamp position in the setup (Michoud et al., 2015; Zannoni et  
446 al., 2015).





447 In the original CRM system, C1 instead of C0 is used as the initial amount of  
448 pyrrole in order to avoid the interference of pyrrole photolysis. The C1 mode, where  
449 dry N<sub>2</sub> and zero air are used meanwhile the mercury lamp is turned on, was measured  
450 every 12 h for a duration of 2 h (Sinha et al., 2008; Hansen et al., 2015). The length of  
451 the duration is necessary to reach the driest conditions possible to minimize residual  
452 OH in the reactor. It should be noted that this procedure can result in an underestimation  
453 of C1, as it is difficult to remove all trace amounts of water molecules from surfaces  
454 and in nitrogen and zero air flowing through the reactor, which is able to produce extra  
455 OH by photolysis (Hansen et al., 2015; Michoud et al., 2015; Zannoni et al., 2015). The  
456 underestimation of C1 will result in an overestimation of OH reactivity. The  
457 significantly smaller photolysis of pyrrole for the ICRM system allows us to measure  
458 the C1 mode differently. Here, the condition that N<sub>2</sub> and zero air are humidified while  
459 the mercury lamp is turned off is regarded as C1. The new C1 mode is able to avoid the  
460 interference resulting from OH radicals produced by photolysis of residual humidity  
461 since the mercury lamp is turned off and OH will not be produced. Besides, the C1  
462 mode in ICRM is measured every 12 h for a duration of 15 min, which also saves time  
463 compared with C1 mode in original CRM.

### 464 **3.5 Humidity difference between zero air and ambient air**

465 The variation of humidity between the C2 (wet zero air) and C3 (ambient air)  
466 measurements could result in a change in OH production rate in the CRM reactor, which  
467 in turn could lead to a C2 measurement not representative of the OH production rate  
468 observed during the C3 measurement (Sinha et al., 2008; Dolgorouky et al., 2012).  
469 Although the use of a catalytic converter or dynamic humidification of zero air can help  
470 to reduce differences in humidity between C2 and C3 modes, small differences still  
471 exist (Michoud et al., 2015). Besides, while catalytic converters can be used to generate  
472 zero air with the same humidity as ambient air, these converters cannot remove NO<sub>x</sub>  
473 species and thus are not suitable for OH reactivity measurements in urban and suburban  
474 areas with high NO<sub>x</sub> conditions (Hansen et al., 2015).

475 To investigate the influence of humidity differences between C2 and C3 on the



476  $R_{\text{meas}}$  in the ICRM system, we test the response of pyrrole concentration to humidity by  
477 introducing zero air with different humidities through arm C at mode C2. The ratio of  
478  $\text{H}_3\text{O}^+(\text{H}_2\text{O})$  to  $\text{H}_3\text{O}^+$  (m37/m19) is selected to represent the level of different humidity.  
479 Figure 7 (a) presents the dependence of pyrrole concentrations on m37/m19 at mode  
480 C2. Pyrrole concentrations slightly decrease with the increase in m37/m19. It must be  
481 noted that this dependence is not due to the humidity dependence of the PTR-MS  
482 sensitivity toward pyrrole, but the change in OH production in the reactor, as the  
483 normalization procedure of pyrrole signal described in Sect. 2.3 was applied to all  
484 pyrrole measurements. The maximum difference of m37/m19 between C2 mode and  
485 C3 mode is about 0.01 corresponding to RH changing by  $\sim 30\%$  (Fig. 7 b), which lead  
486 to pyrrole changed by  $\sim 0.26$  ppbv and thus the  $R_{\text{meas}}$  changed by  $\sim 1.9 \text{ s}^{-1}$  when the  $R_{\text{true}}$   
487 is  $20 \text{ s}^{-1}$ . This result indicates that the influence of humidity change on OH  
488 concentrations and subsequently  $R_{\text{meas}}$  cannot be ignored even though the structure of  
489 arm A was improved to decrease the numbers of photons entering the main body of the  
490 reactor. Therefore, humidity correction is needed to accurately  $R_{\text{meas}}$ . The humidity  
491 difference between C2 and C3 mode can be corrected by the function derived from the  
492 relationship between OH reactivity and m37/m19 (as shown in Fig. 7 a).

### 493 **3.6 Instrument performance in ambient measurements**

494 During the measurement, daily calibration was conducted by introducing a  
495 constant concentration of various VOCs standards (propane, propene or toluene)  
496 through arm C at C2 mode and determining the ratio of  $R_{\text{meas}}$  to  $R_{\text{true}}$  (i.e.  $\alpha_{\text{VOC}}$ ). As shown  
497 in Fig. S9,  $R_{\text{meas}}/R_{\text{true}}$  is relatively stable during the measurement, ranging from 0.60 to  
498 0.70, implying this method has high stability, despite the structural differences of the  
499 VOCs species introduced.

500 Figure 8 (a) presents a time series of  $R_{\text{tot}}$ , calculated OH reactivity ( $R_{\text{cal}}$ ), and  
501 ambient NO.  $R_{\text{tot}}$  was acquired based on Eq. 5, and  $R_{\text{cal}}$  is calculated by the sum of all  
502 measured reactive trace gas concentrations multiplied by their respective reaction rate  
503 coefficients with OH. The new system worked well even at high NO concentrations ( $>$   
504 20 ppbv). The average  $R_{\text{tot}}$  for the entire campaign was  $27 \text{ s}^{-1}$ . The  $R_{\text{tot}}$  is higher than the



505  $R_{\text{cal}}$  by 34% during the campaign, with larger differences observed in the morning and  
506 at night than in the afternoon. As shown in Fig. 8(b), the  $R_{\text{tot}}$  has an obvious diurnal  
507 variation with higher levels at night and morning than that in the afternoon. This is  
508 because air pollutants from anthropogenic emissions were accumulated at night and  
509 morning due to lack of oxidative consumption, whereas were depleted rapidly during  
510 the afternoon due to rising levels of oxidant, i.e. OH radicals. This diurnal pattern of  
511  $R_{\text{tot}}$  is similar to that of the previous measurement results in the Pearl River Delta (Lou  
512 et al., 2010; Yang et al., 2017a) and Beijing (Williams et al., 2016). Overall, the diurnal  
513 variation of the  $R_{\text{true VOC}}$  (calculated by Eq.4) is similar to that of the calculated OH  
514 reactivity of inorganic gas (Fig. 8 b) and the concentration of  $\text{NO}_x$  (Fig. 8 c). A  
515 comparison between the  $R_{\text{tot}}$  determined by the ICRM method and the laser-induced  
516 fluorescence method will be of interest in future studies, particularly because LIF type  
517 systems can also experience difficulties at high NO when OH decay rates are rapid.  
518 Further discussions on the OH reactivity results of this campaign will be given in  
519 another publication.

## 520 **4 Conclusion**

521 In this study, we presented an improved comparative reactivity method (ICRM)  
522 which is suitable for measuring OH reactivity under high-NO conditions. The major  
523 improvements of ICRM compared to the original CRM system are as follows:

524 (1) The  $\text{HO}_2$  and  $\text{RO}_2$  radicals produced from H radicals reacting with  $\text{O}_2$  and OH-  
525 oxidation of pyrrole, respectively, were removed continuously to the largest extent. In  
526 this study, 50 ppbv NO was injected into the ICRM reactor through an additional arm G  
527 between arm A and the reactor. Under this NO level, the interference due to the reaction  
528 of  $\text{HO}_2$  and  $\text{RO}_2$  from pyrrole with NO was minimized.

529 (2) The OH recycling always happens to some extent when sampled VOCs are  
530 introduced into the reactor in the presence of NO, causing the measured OH reactivity  
531 ( $R_{\text{meas}}$ ) deviate from the true OH reactivity ( $R_{\text{true}}$ ). We quantified this effect by  
532 calibrating several representative VOC species, CO and  $\text{SO}_2$  to obtain the slope of  $R_{\text{meas}}$   
533 versus  $R_{\text{true}}$ . Different VOC species produce similar slopes, which are significantly



534 higher than the slopes of CO and SO<sub>2</sub>. Using the average value of the derived slopes of  
535 the different species as a correction factor, we obtained the more accurate  $R_{\text{meas}}$ .  
536 Additionally, the effect of ambient NO on the difference between  $R_{\text{true}}$  and  $R'_{\text{meas}}$  was  
537 quantified.

538 (3) Transforming the structure of the glass reactor to reduce the amount of ultraviolet  
539 light generated by the mercury lamp reaching the main body of the glass reactor. This  
540 effort resulted in eliminating the interference of pyrrole photolysis existed in the  
541 original system. Under this condition, the new C1 mode used was able to avoid the  
542 interference resulting from OH radicals produced by photolysis of residual humidity  
543 and save lots of time compared with the original C1 mode. The ICRM system was  
544 employed in a field campaign to measure OH reactivity and performed well even if  
545 ambient NO concentrations are high.

546

#### 547 **Data availability**

548 The more detailed data can be provided by contacting the corresponding author.

549

#### 550 **Author contributions**

551 WJW and BY came up the idea for the improved CRM. JPQ built the ICRM system  
552 and performed data analysis. WJW, JPQ and BY wrote the manuscript, with  
553 contributions from all other authors. YWP and SHW provided the PTR-TOF-MS and  
554 PAMS data.

555

#### 556 **Competing interests**

557 The author declares that there is no conflict of interest.

558

#### 559 **Acknowledgment**

560 This work was supported by Key-Area Research and Development Program of  
561 Guangdong Province (grant No. 2019B110206001), the National Natural Science  
562 Foundation of China (grant No. 41877302), Guangdong Natural Science Funds for



563 Distinguished Young Scholar (grant No. 2018B030306037), the National Key R&D  
564 Plan of China (grant No. 2019YFE0106300, 2018YFC0213904, 2016YFC0202206),  
565 Guangdong Soft Science Research Program (2019B101001005), and Guangdong  
566 Innovative and Entrepreneurial Research Team Program (grant No. 2016ZT06N263).  
567 This work was also supported by Special Fund Project for Science and Technology  
568 Innovation Strategy of Guangdong Province (Grant No.2019B121205004).



## 569 **References**

- 570 A. Hofzumahaus, H. P. D., J. Callies, U. Platt and D. H. Ehhalt: Tropospheric OH concentration  
571 measurements by laser long-path absorption spectroscopy, *Atmospheric Environment*, 25A, 2017-  
572 2022, 1991.
- 573 Atkinson, R.: Atmospheric chemistry of VOCs and NOx, *Atmospheric Environment*, 36, 2063-2101,  
574 2000.
- 575 Atkinson, R., Aschmann, S. M., Winer, A. M., and Carter, W. P. L.: Rate constants for the gas phase  
576 reactions of OH radicals and O<sub>3</sub>, with pyrrole at 295 ± 1 K and atmospheric pressure, *Atmospheric*  
577 *Environment*, 18, 2105-2107, 1984.
- 578 Atkinson, R., Baulch, D. L., Cox, R. A., Crowley, J. N., Hampson, R. F., Hynes, R. G., Jenkin, M. E.,  
579 Rossi, M. J., and Troe, J.: Evaluated kinetic and photochemical data for atmospheric chemistry:  
580 Volume I – gas phase reactions of O<sub>x</sub>, HO<sub>x</sub>, NO<sub>x</sub> and SO<sub>x</sub> species, *Atmospheric Chemistry and*  
581 *Physics*, 4, 1461-1738, 2004.
- 582 Birks, J. W., Andersen, P. C., Williford, C. J., Turnipseed, A. A., Strunk, S. E., Ennis, C. A., and Mattson,  
583 E.: Folded tubular photometer for atmospheric measurements of NO<sub>2</sub> and NO, *Atmospheric*  
584 *Measurement Techniques*, 11, 2821-2835, doi: 10.5194/amt-11-2821-2018, 2018.
- 585 Cabanas, B., Baeza, M. T., Salgado, S., Martin, P., Taccone, R., and Martinez, E.: Oxidation of  
586 heterocycles in the atmosphere: Kinetic study of their reactions with NO<sub>3</sub> radical, *J. Phys. Chem.*  
587 *A*, 108, 10818-10823, doi: 10.1021/jp046524t, 2004.
- 588 de Gouw, J. and Warneke, C.: Measurements of volatile organic compounds in the earth's atmosphere  
589 using proton-transfer-reaction mass spectrometry, *Mass Spectrom Rev*, 26, 223-257, doi:  
590 10.1002/mas.20119, 2007.
- 591 Dillon, T. J., Tucceri, M. E., Dulitz, K., Horowitz, A., Vereecken, L., and Crowley, J. N.: Reaction of  
592 hydroxyl radicals with C<sub>4</sub>H<sub>5</sub>N (pyrrole): temperature and pressure dependent rate coefficients, *J*  
593 *Phys Chem A*, 116, 6051-6058, doi: 10.1021/jp211241x, 2012.
- 594 Dolgorouky, C., Gros, V., Sarda-Estève, R., Sinha, V., Williams, J., Marchand, N., Sauvage, S., Poulain,  
595 L., Sciare, J., and Bonsang, B.: Total OH reactivity measurements in Paris during the 2010  
596 MEGAPOLI winter campaign, *Atmospheric Chemistry and Physics*, 12, 9593-9612, doi:  
597 10.5194/acp-12-9593-2012, 2012.



- 598 Fuchs, H., Novelli, A., Rolletter, M., Hofzumahaus, A., Pfannerstill, E. Y., Kessel, S., Edtbauer, A.,  
599 Williams, J., Michoud, V., Dusanter, S., Locoge, N., Zannoni, N., Gros, V., Truong, F., Sarda-Esteve,  
600 R., Cryer, D. R., Brumby, C. A., Whalley, L. K., Stone, D., Seakins, P. W., Heard, D. E.,  
601 Schoemaeker, C., Blocquet, M., Coudert, S., Batut, S., Fittschen, C., Thames, A. B., Brune, W. H.,  
602 Ernest, C., Harder, H., Muller, J. B. A., Elste, T., Kubistin, D., Andres, S., Bohn, B., Hohaus, T.,  
603 Holland, F., Li, X., Rohrer, F., Kiendler-Scharr, A., Tillmann, R., Wegener, R., Yu, Z. J., Zou, Q.,  
604 and Wahner, A.: Comparison of OH reactivity measurements in the atmospheric simulation chamber  
605 SAPHIR, *Atmos. Meas. Tech.*, 10, 4023-4053, doi: 10.5194/amt-10-4023-2017, 2017.
- 606 Hansen, R. F., Blocquet, M., Schoemaeker, C., Léonardis, T., Locoge, N., Fittschen, C., Hanoune, B.,  
607 Stevens, P. S., Sinha, V., and Dusanter, S.: Intercomparison of the comparative reactivity method  
608 (CRM) and pump-probe technique for measuring total OH reactivity in an urban environment,  
609 *Atmospheric Measurement Techniques*, 8, 4243-4264, doi: 10.5194/amt-8-4243-2015, 2015.
- 610 Ingham, T., Goddard, A., Whalley, L. K., Furneaux, K. L., Edwards, P. M., Seal, C. P., Self, D. E., Johnson,  
611 G. P., Read, K. A., Lee, J. D., and Heard, D. E.: A flow-tube based laser-induced fluorescence  
612 instrument to measure OH reactivity in the troposphere, *Atmospheric Chemistry and Physics*, 2,  
613 465-477, doi: 10.5194/amt-2-465-2009, 2009.
- 614 Kim, S., Guenther, A., Karl, T., and Greenberg, J.: Contributions of primary and secondary biogenic VOC  
615 to total OH reactivity during the CABINEX (Community Atmosphere-Biosphere Interactions  
616 Experiments)-09 field campaign, *Atmospheric Chemistry and Physics*, 11, 8613-8623, doi:  
617 10.5194/acp-11-8613-2011, 2011.
- 618 Kim, S., Sanchez, D., Wang, M., Seco, R., Jeong, D., Hughes, S., Barletta, B., Blake, D. R., Jung, J.,  
619 Kim, D., Lee, G., Lee, M., Ahn, J., Lee, S. D., Cho, G., Sung, M. Y., Lee, Y. H., Kim, D. B., Kim,  
620 Y., Woo, J. H., Jo, D., Park, R., Park, J. H., Hong, Y. D., and Hong, J. H.: OH reactivity in urban  
621 and suburban regions in Seoul, South Korea - an East Asian megacity in a rapid transition, *Faraday*  
622 *Discuss.*, 189, 231-251, doi: 10.1039/c5fd00230c, 2016.
- 623 Kovacs, T. A. and Brune, W. H.: Total OH Loss Rate Measurement, *Journal of Atmospheric Chemistry*,  
624 39, 105-122, doi: 10.1023/A:1010614113786, 2001.
- 625 Kovacs, T. A., Brune, W. H., Harder, H., Martinez, M., Simpas, J. B., Frost, G. J., Williams, E., Jobson,  
626 T., Stroud, C., Young, V., Fried, A., and Wert, B.: Direct measurements of urban OH reactivity



- 627 during Nashville SOS in summer 1999, *J Environ Monit*, 5, 68-74, doi: 10.1039/b204339d, 2003.
- 628 Kumar, V., Chandra, B. P., and Sinha, V.: Large unexplained suite of chemically reactive compounds  
629 present in ambient air due to biomass fires, *Sci Rep*, 8, 626, doi: 10.1038/s41598-017-19139-3,  
630 2018.
- 631 Kumar, V. and Sinha, V.: VOC–OHM: A new technique for rapid measurements of ambient total OH  
632 reactivity and volatile organic compounds using a single proton transfer reaction mass spectrometer,  
633 *International Journal of Mass Spectrometry*, 374, 55-63, doi: 10.1016/j.ijms.2014.10.012, 2014.
- 634 Lou, S., Holland, F., Rohrer, F., Lu, K., Bohn, B., Brauers, T., Chang, C. C., Fuchs, H., Häseler, R., Kita,  
635 K., Kondo, Y., Li, X., Shao, M., Zeng, L., Wahner, A., Zhang, Y., Wang, W., and Hofzumahaus, A.:  
636 Atmospheric OH reactivities in the Pearl River Delta – China in summer 2006: measurement and  
637 model results, *Atmospheric Chemistry and Physics*, 10, 11243-11260, doi: 10.5194/acp-10-11243-  
638 2010, 2010.
- 639 Michoud, V., Hansen, R. F., Locoge, N., Stevens, P. S., and Dusanter, S.: Detailed characterizations of  
640 the new Mines Douai comparative reactivity method instrument via laboratory experiments and  
641 modeling, *Atmospheric Measurement Techniques*, 8, 3537-3553, doi: 10.5194/amt-8-3537-2015,  
642 2015.
- 643 Nölscher, A. C., Bourtsoukidis, E., Bonn, B., Kesselmeier, J., Lelieveld, J., and Williams, J.: Seasonal  
644 measurements of total OH reactivity emission rates from Norway spruce in 2011, *Biogeosciences*,  
645 10, 4241-4257, doi: 10.5194/bg-10-4241-2013, 2013.
- 646 Nölscher, A. C., Butler, T., Auld, J., Veres, P., Muñoz, A., Taraborrelli, D., Vereecken, L., Lelieveld, J.,  
647 and Williams, J.: Using total OH reactivity to assess isoprene photooxidation via measurement and  
648 model, *Atmospheric Environment*, 89, 453-463, doi: 10.1016/j.atmosenv.2014.02.024, 2014.
- 649 Nölscher, A. C., Sinha, V., Bockisch, S., Klupfel, T., and Williams, J.: Total OH reactivity measurements  
650 using a new fast Gas Chromatographic Photo-Ionization Detector (GC-PID), *Atmos. Meas. Tech.*,  
651 5, 2981-2992, doi: 10.5194/amt-5-2981-2012, 2012a.
- 652 Nölscher, A. C., Williams, J., Sinha, V., Custer, T., Song, W., Johnson, A. M., Axinte, R., Bozem, H.,  
653 Fischer, H., Pouvesle, N., Phillips, G., Crowley, J. N., Rantala, P., Rinne, J., Kulmala, M., Gonzales,  
654 D., Valverde-Canossa, J., Vogel, A., Hoffmann, T., Ouwersloot, H. G., de Arellano, J. V. G., and  
655 Lelieveld, J.: Summertime total OH reactivity measurements from boreal forest during HUMPPA-





- 656 COPEC 2010, *Atmospheric Chemistry and Physics*, 12, 8257-8270, doi: 10.5194/acp-12-8257-2012,  
657 2012b.
- 658 Pfannerstill, E. Y., Nölscher, A. C., Yáñez-Serrano, A. M., Bourtsoukidis, E., Keßel, S., Janssen, R. H.  
659 H., Tsokankunku, A., Wolff, S., Sörgel, M., Sá, M. O., Araújo, A., Walter, D., Lavrič, J., Dias-Júnior,  
660 C. Q., Kesselmeier, J., and Williams, J.: Total OH Reactivity Changes Over the Amazon Rainforest  
661 During an El Niño Event, *Frontiers in Forests and Global Change*, 1, doi: 10.3389/ffgc.2018.00012,  
662 2018.
- 663 Pfannerstill, E. Y., Reijrink, N. G., Edtbauer, A., Ringsdorf, A., Zannoni, N., Araújo, A., Ditas, F.,  
664 Holanda, B. A., Sá, M. O., Tsokankunku, A., Walter, D., Wolff, S., Lavrič, J. V., Pöhlker, C., Sörgel, M.,  
665 and Williams, J.: Total OH reactivity over the Amazon rainforest: variability with temperature, wind,  
666 rain, altitude, time of day, season, and an overall budget closure, *Atmospheric Chemistry and*  
667 *Physics Discussions*, doi: 10.5194/acp-2020-752, 2020. doi: 10.5194/acp-2020-752, 2020.
- 668 Pfannerstill, E. Y., Wang, N., Edtbauer, A., Bourtsoukidis, E., Crowley, J. N., Dienhart, D., Eger, P. G.,  
669 Ernle, L., Fischer, H., Hottmann, B., Paris, J.-D., Stönnner, C., Tadic, I., Walter, D., Lelieveld, J., and  
670 Williams, J.: Shipborne measurements of total OH reactivity around the Arabian Peninsula and its  
671 role in ozone chemistry, *Atmospheric Chemistry and Physics*, 19, 11501-11523, doi: 10.5194/acp-  
672 19-11501-2019, 2019.
- 673 Praplan, A. P., Pfannerstill, E. Y., Williams, J., and Hellen, H.: OH reactivity of the urban air in Helsinki,  
674 Finland, during winter, *Atmos. Environ.*, 169, 150-161, doi: 10.1016/j.atmosenv.2017.09.013,  
675 2017a.
- 676 Praplan, A. P., Pfannerstill, E. Y., Williams, J., and Hellén, H.: OH reactivity of the urban air in Helsinki,  
677 Finland, during winter, *Atmospheric Environment*, 169, 150-161, doi:  
678 10.1016/j.atmosenv.2017.09.013, 2017b.
- 679 Praplan, A. P., Tykkä, T., Chen, D., Boy, M., Taipale, D., Vakkari, V., Zhou, P., Petäjä, T., and Hellén, H.:  
680 Long-term total OH reactivity measurements in a boreal forest, *Atmospheric Chemistry and Physics*,  
681 19, 14431-14453, doi: 10.5194/acp-19-14431-2019, 2019a.
- 682 Praplan, A. P., Tykkä, T., Chen, D., Boy, M., Taipale, D., Vakkari, V., Zhou, P. T., Petaja, T., and Hellen,  
683 H.: Long-term total OH reactivity measurements in a boreal forest, *Atmospheric Chemistry and*  
684 *Physics*, 19, 14431-14453, doi: 10.5194/acp-19-14431-2019, 2019b.



- 685 Roger Atkinson, J. A.: Atmospheric Degradation of Volatile Organic Compounds, *Chem. Rev.*, 103,  
686 4605-4638, 2003.
- 687 Sadanaga, Y., Yoshino, A., Kato, S., and Kajii, Y.: Measurements of OH Reactivity and Photochemical  
688 Ozone Production in the Urban Atmosphere, *Environ. Sci. Technol.*, 39, 8847-8852, doi:  
689 10.1021/es049457p 2005.
- 690 Sadanaga, Y., Yoshino, A., Watanabe, K., Yoshioka, A., Wakazono, Y., Kanaya, Y., and Kajii, Y.:  
691 Development of a measurement system of OH reactivity in the atmosphere by using a laser-induced  
692 pump and probe technique, *Review of Scientific Instruments*, 75, 2648-2655, doi:  
693 10.1063/1.1775311, 2004.
- 694 Sinha, V., Custer, T. G., Kluepfel, T., and Williams, J.: The effect of relative humidity on the detection of  
695 pyrrole by PTR-MS for OH reactivity measurements, *International Journal of Mass Spectrometry*,  
696 282, 108-111, doi: 10.1016/j.ijms.2009.02.019, 2009.
- 697 Sinha, V., Williams, J., Crowley, J. N., and Lelieveld, J.: The Comparative Reactivity Method-a new tool  
698 to measure total OH Reactivity in ambient air, *Atmospheric Chemistry and Physics*, 8, 2213-2227,  
699 doi: 10.5194/acp-8-2213-2008, 2008.
- 700 Sinha, V., Williams, J., Diesch, J. M., Drewnick, F., Martinez, M., Harder, H., Regelin, E., Kubistin, D.,  
701 Bozem, H., Hosaynali-Beygi, Z., Fischer, H., Andrés-Hernández, M. D., Kartal, D., Adame, J. A.,  
702 and Lelieveld, J.: Constraints on instantaneous ozone production rates and regimes during  
703 DOMINO derived using in-situ OH reactivity measurements, *Atmospheric Chemistry and Physics*,  
704 12, 7269-7283, doi: 10.5194/acp-12-7269-2012, 2012.
- 705 Sinha, V., Williams, J., Lelieveld, J., Ruuskanen, T. M., Kajos, M. K., Patokoski, J., Hellen, H., Hakola,  
706 H., Mogensen, D., Boy, M., Rinne, J., and Kulmala, M.: OH Reactivity Measurements within a  
707 Boreal Forest: Evidence for Unknown Reactive Emissions, *Environmental Science & Technology*,  
708 44, 6614-6620, doi: 10.1021/es101780b, 2010.
- 709 Tan, Z. F., Lu, K. D., Hofzumahaus, A., Fuchs, H., Bohn, B., Holland, F., Liu, Y. H., Rohrer, F., Shao,  
710 M., Sun, K., Wu, Y. S., Zeng, L. M., Zhang, Y. S., Zou, Q., Kiendler-Scharr, A., Wahner, A., and  
711 Zhang, Y. H.: Experimental budgets of OH, HO<sub>2</sub>, and RO<sub>2</sub> radicals and implications for ozone  
712 formation in the Pearl River Delta in China 2014, *Atmospheric Chemistry and Physics*, 19, 7129-  
713 7150, doi: 10.5194/acp-19-7129-2019, 2019.



- 714 Wang, M., Zeng, L., Lu, S., Shao, M., Liu, X., Yu, X., Chen, W., Yuan, B., Zhang, Q., Hu, M., and Zhang,  
715 Z.: Development and validation of a cryogen-free automatic gas chromatograph system (GC-  
716 MS/FID) for online measurements of volatile organic compounds, *Anal. Methods*, 6, 9424-9434,  
717 doi: 10.1039/c4ay01855a, 2014a.
- 718 Wang, Y., Ying, Q., Hu, J., and Zhang, H.: Spatial and temporal variations of six criteria air pollutants in  
719 31 provincial capital cities in China during 2013-2014, *Environ Int*, 73, 413-422, doi:  
720 10.1016/j.envint.2014.08.016, 2014b.
- 721 Williams, J., Keßel, S. U., Nölscher, A. C., Yang, Y., Lee, Y., Yáñez-Serrano, A. M., Wolff, S.,  
722 Kesselmeier, J., Klüpfel, T., Lelieveld, J., and Shao, M.: Opposite OH reactivity and ozone cycles  
723 in the Amazon rainforest and megacity Beijing: Subversion of biospheric oxidant control by  
724 anthropogenic emissions, *Atmospheric Environment*, 125, 112-118, doi:  
725 10.1016/j.atmosenv.2015.11.007, 2016.
- 726 Wolfe, G. M., Marvin, M. R., Roberts, S. J., Travis, K. R., and Liao, J.: The Framework for 0-D  
727 Atmospheric Modeling (F0AM) v3.1, *Geoscientific Model Development*, 9, 3309-3319, doi:  
728 10.5194/gmd-9-3309-2016, 2016.
- 729 Wu, Y., Yang, Y. D., Shao, M., and Lu, S. H.: Missing in total OH reactivity of VOCs from gasoline  
730 evaporation, *Chin. Chem. Lett.*, 26, 1246-1248, doi: 10.1016/j.ccllet.2015.05.047, 2015.
- 731 Yang, Y., Shao, M., Keßel, S., Li, Y., Lu, K., Lu, S., Williams, J., Zhang, Y., Zeng, L., Nölscher, A. C.,  
732 Wu, Y., Wang, X., and Zheng, J.: How the OH reactivity affects the ozone production efficiency:  
733 case studies in Beijing and Heshan, China, *Atmospheric Chemistry and Physics*, 17, 7127-7142, doi:  
734 10.5194/acp-17-7127-2017, 2017a.
- 735 Yang, Y., Shao, M., Keßel, S., Li, Y., Lu, K., Lu, S., Williams, J., Zhang, Y., Zeng, L., Nölscher, A. C.,  
736 Wu, Y., Wang, X., and Zheng, J.: How the OH reactivity affects the ozone production efficiency:  
737 case studies in Beijing and Heshan, China, *Atmos. Chem. Phys.*, 17, 7127-7142, doi: 10.5194/acp-  
738 17-7127-2017, 2017b.
- 739 Yang, Y., Shao, M., Wang, X., Nölscher, A. C., Kessel, S., Guenther, A., and Williams, J.: Towards a  
740 quantitative understanding of total OH reactivity: A review, *Atmospheric Environment*, 134, 147-  
741 161, doi: 10.1016/j.atmosenv.2016.03.010, 2016.
- 742 Yuan, B., Koss, A. R., Warneke, C., Coggon, M., Sekimoto, K., and de Gouw, J. A.: Proton-Transfer-



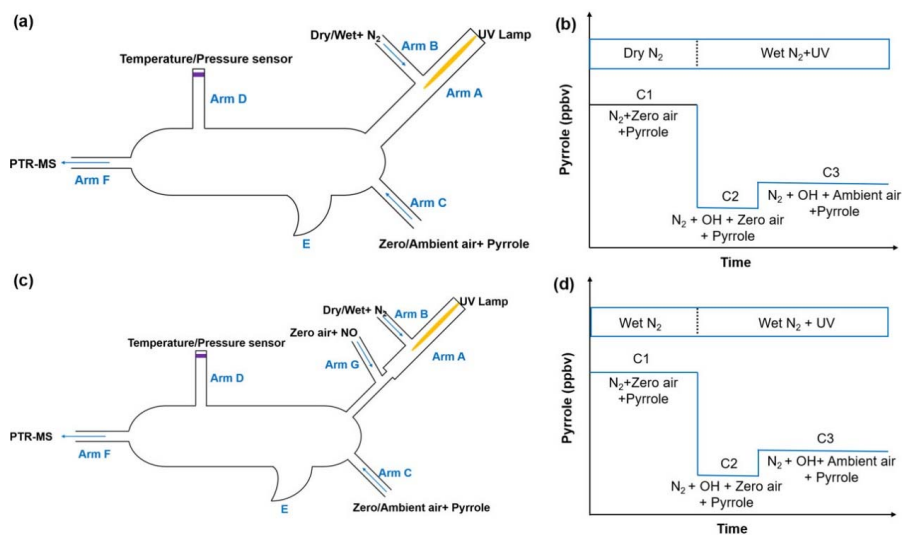
743           Reaction Mass Spectrometry: Applications in Atmospheric Sciences, *Chem Rev*, 117, 13187-13229,  
744           doi: 10.1021/acs.chemrev.7b00325, 2017.

745   Zannoni, N., Dusanter, S., Gros, V., Esteve, R. S., Michoud, V., Sinha, V., Locoge, N., and Bonsang, B.:  
746           Intercomparison of two comparative reactivity method instruments in the Mediterranean basin  
747           during summer 2013, *Atmos. Meas. Tech.*, 8, 3851-3865, doi: 10.5194/amt-8-3851-2015, 2015.

748   Zannoni, N., Gros, V., Lanza, M., Sarda, R., Bonsang, B., Kalogridis, C., Preunkert, S., Legrand, M.,  
749           Jambert, C., Boissard, C., and Lathiere, J.: OH reactivity and concentrations of biogenic volatile  
750           organic compounds in a Mediterranean forest of downy oak trees, *Atmospheric Chemistry and  
751           Physics*, 16, 1619-1636, doi: 10.5194/acp-16-1619-2016, 2016.

752   Zannoni, N., Gros, V., Sarda Esteve, R., Kalogridis, C., Michoud, V., Dusanter, S., Sauvage, S., Locoge,  
753           N., Colomb, A., and Bonsang, B.: Summertime OH reactivity from a receptor coastal site in the  
754           Mediterranean Basin, *Atmospheric Chemistry and Physics*, 17, 12645-12658, doi: 10.5194/acp-17-  
755           12645-2017, 2017.

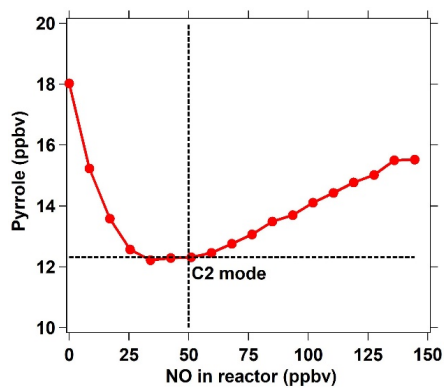
756



757

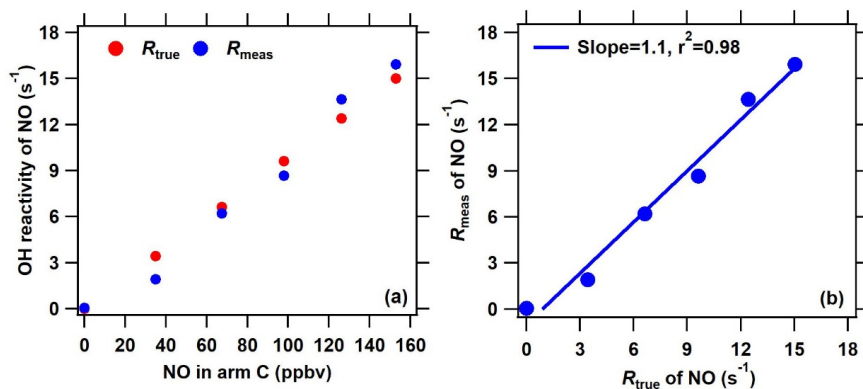
758 **Figure 1.** Schematic and work mode of the original CRM method (Sinha et al., 2008,

759 a and b) and the ICRM method (this study, c and d).



760

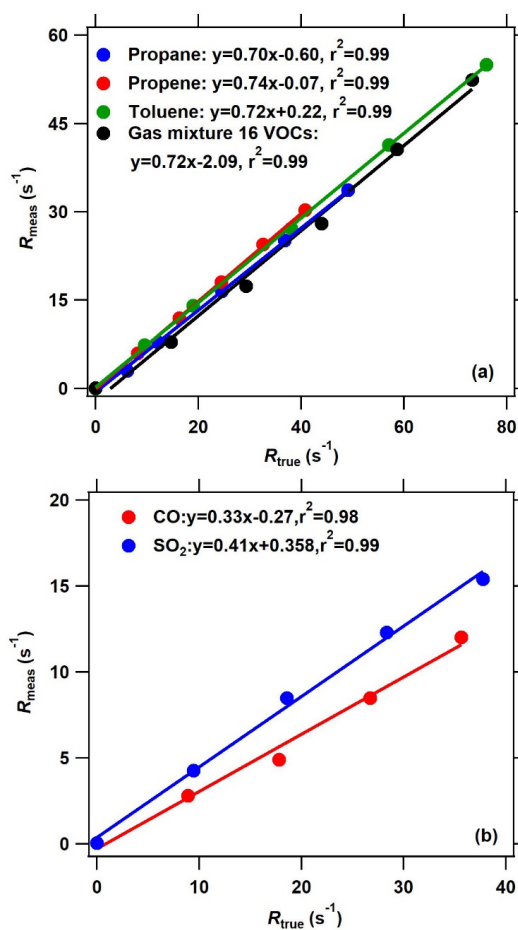
761 **Figure 2.** The response of pyrrole concentration to different NO concentrations  
762 introduced through arm G into the reactor. For the ICRM system, the C2 mode is  
763 corresponding to the pyrrole concentration = 12.31 ppbv at NO = 50 ppbv where the  
764 HO<sub>2</sub> radicals were removed constantly.



765

766 **Figure 3.** Comparison of measured and true OH reactivity of NO at different NO  
767 concentrations introduced through arm C. The measured OH reactivity of NO was  
768 calculated based on the new C2 mode shown in Fig. 2 in the ICRM system.

769

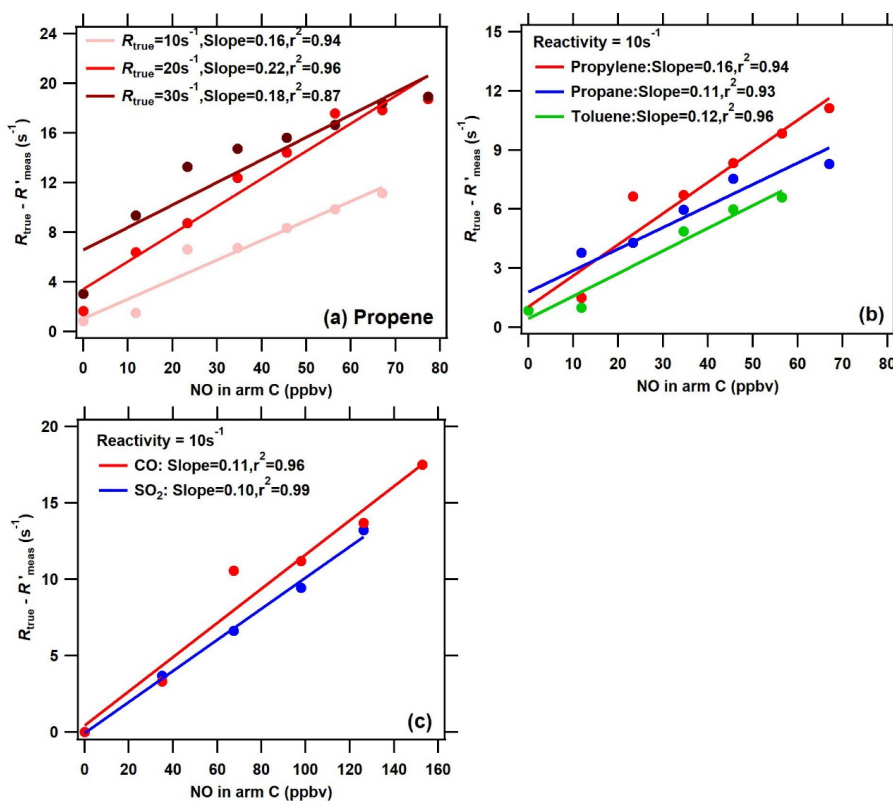


770

771 **Figure 4.** The OH reactivity calibration of the improved CRM system using different  
772 standard gases. (a) The calibrating results of organic species including propane,  
773 propene toluene, and mixture gases of 16 VOC species through arm C. (b) The  
774 calibrating results of inorganic species including CO and SO<sub>2</sub>. The measured OH  
775 reactivity was calculated based on the C2 mode shown in Fig. 2 in the ICRM system.

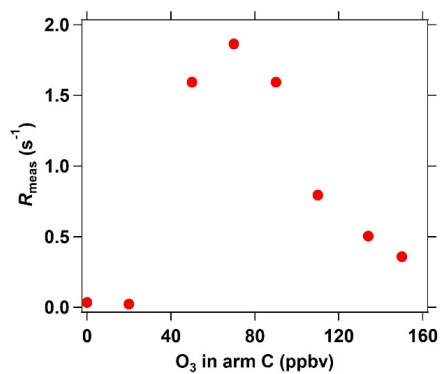
776





777

778 **Figure 5.** The difference between true OH reactivity ( $R_{\text{true}}$ ) and the corrected measured  
 779 OH reactivity ( $R'_{\text{meas}}$ ) using the calibration factor  $\alpha_1$  ( $R'_{\text{meas}} = (\frac{1}{\alpha_{\text{VOC}}} * R_{\text{meas}})$ ) as a  
 780 function of NO concentrations in arm C in the conditions of (a) different levels of VOCs  
 781 reactivity for the same species (propylene), (b) different VOCs species for the same  
 782 OH reactivity level ( $10 \text{ s}^{-1}$ ), and (c) different inorganic species (Red: CO; Blue: SO<sub>2</sub>)  
 783 for the same OH reactivity level ( $10 \text{ s}^{-1}$ ). Note that NO, CO, SO<sub>2</sub>, and VOCs were  
 784 introduced into the reactor through arm C.  
 785



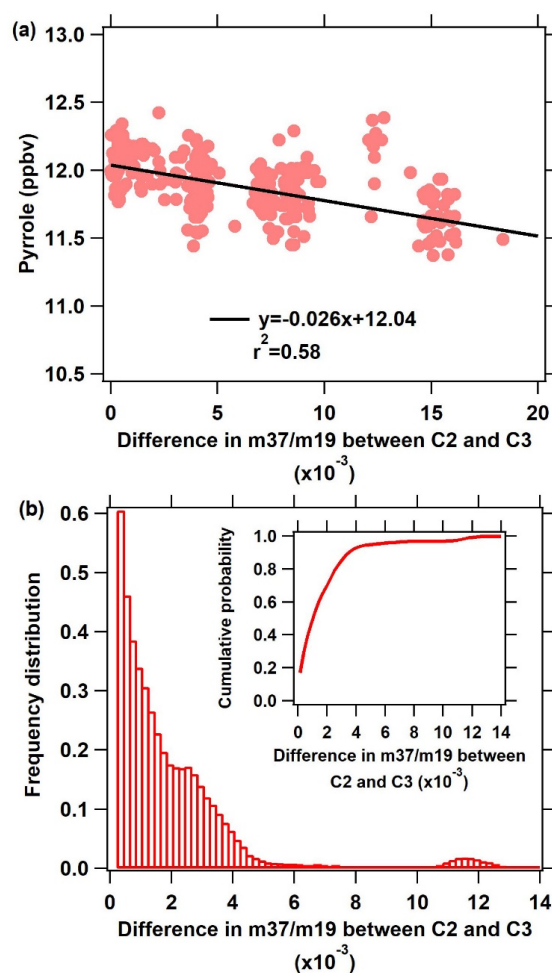
786

787 **Figure 6.** Interference of different O<sub>3</sub> concentration (introduced into the reactor through

788 arm C) on measured OH reactivity in the ICRM system.



789

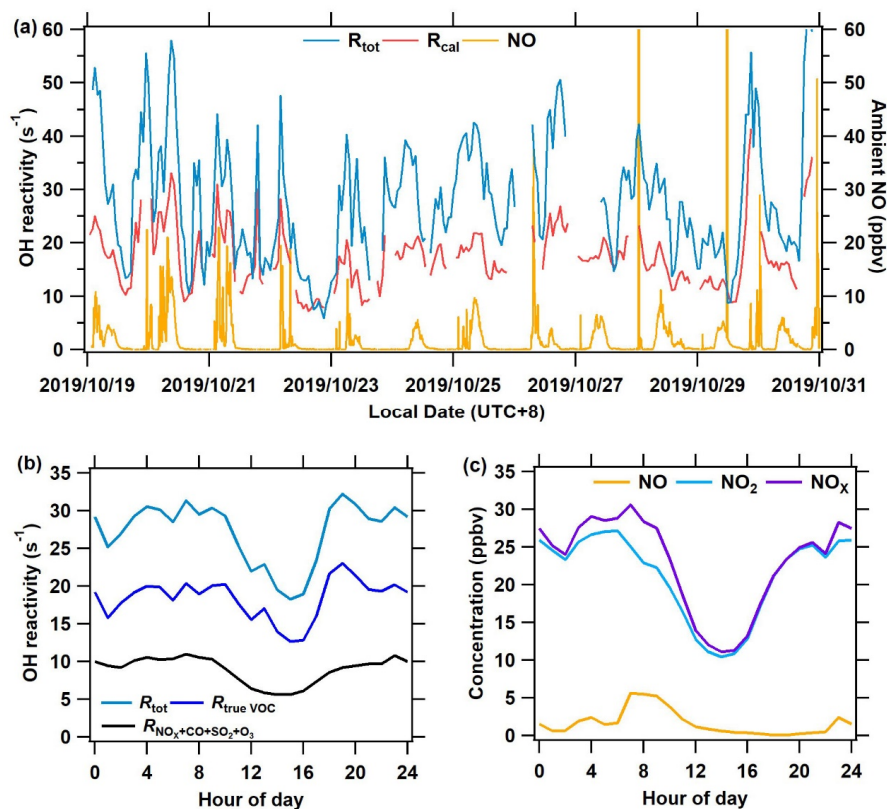


790

791 **Figure 7.** (a) Pyrrole concentration during zero air measurements (C2) as a function of  
792 the difference in m37/m19 between C2 and C3 humidity indicator (m37/m19). (b)  
793 Frequency distribution of the difference in m37/m19 between C2 and C3 during the  
794 measurement.

795

796



797

798 **Figure 8.** The measurement results of OH reactivity and ambient NO at the Heshan site  
799 from October 19 to October 31, 2019. (a) The time series of total OH reactivity ( $R_{tot}$ ),  
800 calculated reactivity ( $R_{cal}$ ), and ambient NO concentration; (b) Mean diurnal profile of  
801 OH reactivity of  $R_{true\ VOC}$ ,  $R_{NO_x+CO+SO_2+O_3}$ , and  $R_{tot}$ ; (c) Mean diurnal profiles of  
802 measured NO,  $NO_2$ , and  $NO_x$ .